*Proceedings of the Twenty-eighth (2018) International Ocean and Polar Engineering Conference*
*Sapporo, Japan, June 10-15, 2018*


*ISBN 978-1-880653-87-6; ISSN 1098-6189*

# Numerical Study of the Effects of Grid Scale on Bow Wave Breaking

*Zhen Ren, Jianhua Wang, Decheng Wan**

Collaborative Innovation Center for Advanced Ship and Deep-Sea Exploration, State Key Laboratory of Ocean Engineering, School of Naval Architecture, Ocean and Civil Engineering, Shanghai Jiao Tong University, Shanghai, China
*Corresponding author

ABSTRACT

In order to study the influences of grid scale on the wave breaking, three different computational grids are adopted in the simulation of the bow wave breaking of KCS at $Fr$=0.35. RANS approach coupled with high resolution VOF technique is used to resolve the free surface. It is found that when the ratio of the grid size to the hull length is about 1.5e-3, the breaking of bow wave can be better resolved. The sensitivity of bow wave breaking to the grid scale in $x$ and $y$ direction is the same as that in $z$ direction.

KEY WORDS: Grid scale; high-speed surface ship; bow wave breaking; naoe-FOAM-SJTU solver; ship hydrodynamics.

## INTRODUCTION

The overturning and breaking of bow and shoulder waves, known as white water, is a complex phenomenon with many small-scale features, such as, air entrainment, capillary wave, which are always observed when the ship advances at high speed on the sea. The mechanism of bow wave breaking and its impact on ship hydrodynamic performance have not been well understood so it is of great significance to study the ship bow breaking waves. At present, the hydrodynamic experiment is the main way to study the ship bow wave breaking. In the formation of ship bow wave, the considerable vorticity originally at the toe was generated near the free surface. And the powerful counter-rotating vorticity concentrated near the wave crest was found by Dong et al. (1997). Being similar to the study of Dong, Roth et al. (1999) utilized particle image velocimetry to measure the flow structure and turbulence within the bow wave of DDG-51 model 5422. In the measurements, they also found that the negative vorticity originated at the toe of the wave while the positive vorticity was generated on the crest of the wave. In addition, they discovered that the great energy losses were experienced at the toe. Waniewski et al. (2002) studied the bow wave dynamics by using a deflecting plate, instead of a ship, in a supercritical flow in the flume experiments. In their study, the experimental data was compared with the results of Ogilvie (1972). The results demonstrated that the bow waves formed in the flume experiments with the depth equal to the draft was similar to the results obtained in towing tank experiments for the same Froude number. Duncan (1983) studied the breaking and non-breaking wave resistance of a 2-D hydrofoil via the experiments in which he found the drag associated with breaking was more than 3 times the drag theoretically obtained with non-breaking waves.

As a main way to study the bow wave breaking, the experiments provided rich and reliable data for the numerical method. But the rapidly developing computational fluid dynamics (CFD) also provides a reliable and robust tool to study the wave breaking and more detailed information in flow field can be obtained through this method. Wilson et al. (2006) utilized the URANS code, CFDSHIP-IOWA, to study the bow and stern wave breaking of the high-speed ship (R/V Athena I) at different Froude numbers ($Fr$ = 0.25, 0.43 and 0.62). In their study, single-phase level set method was adopted to capture free surface and the structured overset grids were used to refine the local regions near the bow and transom waves. Olivieri et al. (2007) studied the scars and vortices induced by bow and shoulder wave breaking of DTMB 5415 in the experiments with CFD data being the supplement to better understand the flow under the bow and shoulder wave. Marrone et al. (2011) used a 2D+t SPH model to analyze the breaking wave pattern of the vessel DTMB 5365, and the overturning and breaking of bow wave were captured clearly. Marrone et al. (2012)

developed a 3D SPH solver to simulate the bow wave breaking of Alliance vessels. The results achieved by the solver were compared with the experimental measurements and numerical results from RANS simulation in which the level set method was applied to resolve the free surface. Wang and Wan (2017) used the solver naoe-FOAM-SJTU, developed on OpenFOAM, to analyze the bow, shoulder and stern wave breaking of benchmark ship model DTMB 5415 at *Fr*=0.35, 0.41. The bow and stern wave breaking were captured through the numerical scheme in which there were 18.7million grids. The wake fields in *x*, *y* and *z* direction obtained in the numerical simulations were in good agreement with the experiment data. When the ship advances under extreme sea conditions, the wave breaking caused by the slamming was also observed in the studies of Liu et al. (2017a, b). Furthermore, the complex phenomena of overturning and breaking of wave are always observed in the nearshore area. In the studies of Xia and Wan (2017a), the effects of the wave steepness on wave breaking over submerged reef were revealed in their numerical simulations via the viscous flow solver, naoe-FOAM_SJTU. In their studies (Xia et al, 2017b) on the hydrodynamic characteristics of floating platform, the profile and properties of the wave breaking was clearly depicted.

In the present work, the grid effects on the bow wave breaking of the KRISO Container Ship (KCS) are studied. The open source software, OpenFOAM, is used to complete the numerical simulations. In the simulations, RANS approach coupled with high resolution VOF technique is used to resolve the free surface. The main framework of this paper goes as following. The first part is the numerical methods, where VOF method and numerical schemes are presented. The second part is the geometry model and test conditions. Then comes the grid generation, the results and analysis part where wave breaking simulations obtained by different grid schemes are present. Finally, the conclusion of this paper is drawn.

## NUMERICAL METHOD

### Governing Equations

In the simulations, the multi-phase CFD solver, interFoam, is applied to solve the Reynolds Averaged Navier-Stokes (RANS) equations for unsteady turbulent flows and VOF method is used to capture free surface around the complex hull. URANS equations including the mass conservation equation and the momentum conservation equation are written as:

$$\nabla \cdot \mathbf{U} = 0 \tag{1}$$

$$\frac{\partial \rho \mathbf{U}}{\partial t} + \nabla \cdot \left(\rho(\mathbf{U}-\mathbf{U}_g)\mathbf{U}\right) = -\nabla p_d - \mathbf{g}\cdot\mathbf{x}\nabla\rho + \nabla\cdot(\mu_{eff}\nabla\mathbf{U}) + (\nabla\mathbf{U})\cdot\nabla\mu_{eff} + f_\sigma \tag{2}$$

where $\mathbf{U}$ is fluid velocity field and $\mathbf{U}_g$ is the grid velocity; $p_d$ represents the dynamic pressure; $\rho$ is the mixture density; $\boldsymbol{g}$ is the gravity acceleration; $\mu_{eff}$ is effective dynamic viscosity, in which $v$ and $v_t$ are kinetic and eddy viscosity, respectively, and $v_t$ is obtained from turbulence model. $f_\sigma$ is surface tension term. The two-equation shear stress transport model, SST $k$-$\omega$ model (Menter et al., 2003), is selected to solve the Reynolds stress. $k$ denotes turbulence kinetic energy and $\omega$ denotes dissipation rate. The turbulence model combines the advantages of the standard $k$-$\varepsilon$ model and $k$-$\omega$ model to make sure that the free surface is not influenced and ensure the accuracy and reliability of the solution at the wall.

### VOF Method and Surface Tension

Here the Volume of Fluid (VOF) method with artificial compression (Weller and Weller, 2008) is used to capture the free surface. Details of the VOF solution procedure as implemented in OpenFOAM are described by Rusche (2003). The transport equation is expressed as:

$$\frac{\partial \alpha}{\partial t} + \nabla\cdot\left(\rho(\mathbf{U}-\mathbf{U}_g)\alpha\right) + \nabla\cdot(\mathbf{U}_r(1-\alpha)\alpha) = 0 \tag{3}$$

where $\alpha$ is the volume of fraction, indicating the relative proportion of fluid in each cell and its value is always between zero and one:

$$\begin{cases} \alpha = 0 & air \\ \alpha = 1 & water \\ 0 < \alpha < 1 & interface \end{cases} \tag{4}$$

In Equation (3), $\mathbf{U}_r$ is the velocity field used to compress the interface, which can simulate the large deformation of free surface. But it takes effect only on the surface interface due to the term (1-$\alpha$) $\alpha$. The expression of this term can be found in Berberović (2009).

The surface tension plays an important role for the breaking and non-breaking waves since the pressure jump mainly depends on the curvature of the free surface. In order to capture the free surface accurately, the surface tension must be taken into consideration. The surface tension term mentioned in Equation (2) is expressed as:

$$f_\sigma = \sigma\kappa\nabla\alpha \tag{5}$$

where $\sigma$ stands for the surface tension, $\kappa$ is the curvature of free surface and it is defined as:

$$\kappa = -\nabla\cdot\mathbf{n} = -\frac{\sum_f \mathbf{S}_f\cdot\mathbf{n}_f}{V_i} \tag{6}$$

where $V_i$ represents the volume of cell $i$, $\sum_f \mathbf{S}_f$ stands for the sum of value on each face of cell.

In the present work, Finite Volume Method (FVM) with All-hexahedral unstructured grids is used to discretize the

computational domain and transform the information from physical space into computational space. The algorithm PISO-SIMPLE (PIMPLE) applied in the numerical simulation merges the advantages of the Semi-Implicit Method for Pressure-Linked Equations (SIMPLE) algorithm that allows to couple the Navier-Stokes equations with an iterative procedure and the Pressure Implicit Splitting Operator (PISO) algorithm that complete the pressure-velocity correction.

## GEOMETRY MODEL AND GRID GENERATION

### Geometry Model

As a full-formed hull, the wave breaking of KRISO Container Ship (KCS) has attracted many scholars. The geometry model that is the 6.0702 m replica with rudder in numerical simulations is shown in Fig. 1, and its principle parameters are listed in Table 1. Extensive experiments have been conducted for the ship model under various Froude numbers except for Fr above 0.30. Although the design speed of KCS is 24knots, Fr=0.26, the phenomena of bow wave breaking will be observed clearly at Fr=0.35 according to the previous numerical study. So, the present numerical simulations are conducted at Fr=0.35. In the present study, the model is fixed without the sinkage and trim being taken into account.

Fig. 1 Geometry model of KCS (Case 2.10)

Table 1 Principle dimensions of KCS

| Main particulars | | Full scale | Model scale |
|---|---|---|---|
| Length between perpendiculars | $L_{pp}$ (m) | 230 | 6.0702 |
| Maximum beam of waterline | $B_{WL}$ (m) | 32.2 | 0.8498 |
| Draft | $T$ (m) | 10.8 | 0.2850 |
| Displacement volume | $\Delta$ (m$^3$) | 52030 | 0.9565 |
| Wetted surface area (with rudder) | $S_0$ (m$^2$) | 9645 | 6.7182 |

### Grid Generation

Due to the high computational costs and fixed ship model condition, only half of the computational domain is adopted for the numerical simulations. Fig. 2 shows the computational domain and the boundary conditions.

All-hexahedral unstructured grid adopted in the present simulations is generated by the software, *Hexpress*. The grid number in $x$, $y$, $z$ direction is 100×30×45, respectively. To better resolve the bow wave breaking and free surface wave pattern, several blocks are adopted to refine the regions around the hull, bow and local free surface, as shown in Fig. 3. Three grid schemes are obtained via the refinement in different directions to study the grid scale effects on the bow wave breaking, as listed in
Table 2. The scale of the size of the highest-level refinement region to $L_{pp}$ is about 1.56e-3. Block 1 that is adopted in three grid schemes is the transition zone to refine the grid around the hull surface, while Block 2-3 are used to refine the grid near free surface. The 16.1 million grids scheme is achieved via the refinement in $z$ direction based on the 13.5 million grids scheme. Through the refinement in $x$ and $y$ directions based on the 16.1 million grids scheme, the 18.3 million grids scheme is obtained. Fig. 4 presents the profile of grid distribution. Fig. 5 shows the bow grid distribution via the refinement in $z$ direction and Fig. 6 presents the bow grid distribution via the refinement in $x$ and $y$ direction.

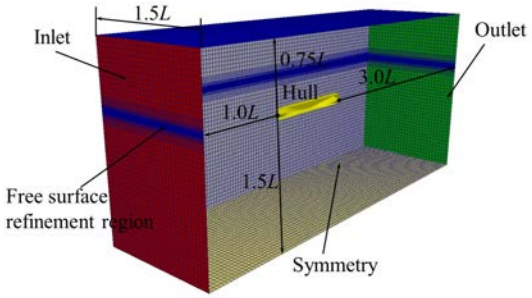


Fig. 2 Domain and boundary conditions.

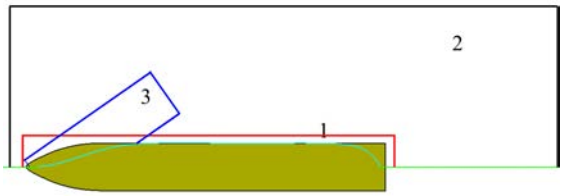


Fig. 3 Refinement regions.

Table 2 Grid refinement strategy

| Total | No. | Refinement level ($x$, $y$, $z$) | Ratio($/L_{pp}$) ($\times 10^{-3}$) |
|---|---|---|---|
| | 1 | 3×3×3 | 6.25×6.25×6.25 |
| 13.5Million | 2 | 4×4×4 | 3.125×3.125×3.125 |
| | 3 | - | - |
| 16.1Million | 2 | 4×4×5 | 3.125×3.125×1.5625 |
| | 3 | - | - |
| 18.3Million | 2 | 4×4×5 | 3.125×3.125×1.5625 |
| | 3 | 5×5×5 | 1.5625×1.5625×1.5625 |

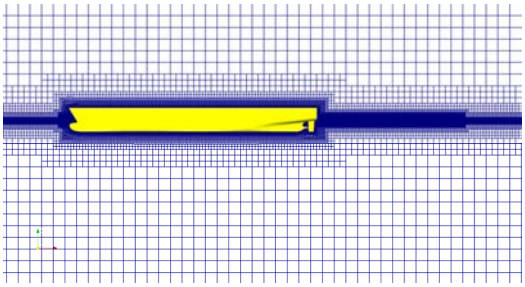

Fig. 4 Profile of grid distribution

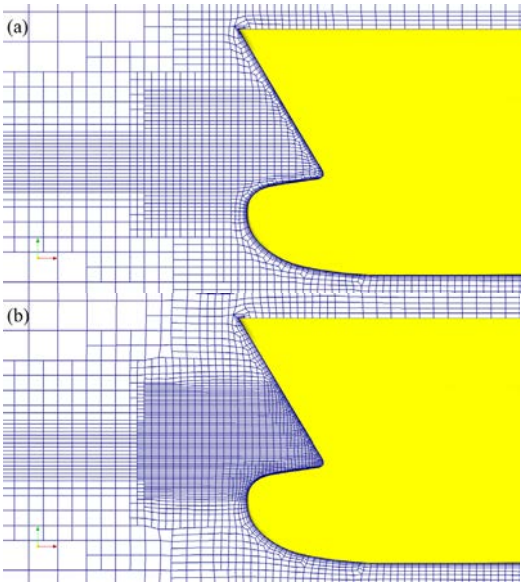


Fig. 5 Grid refinement in z direction (a: 13.5million; b: 16.1million).

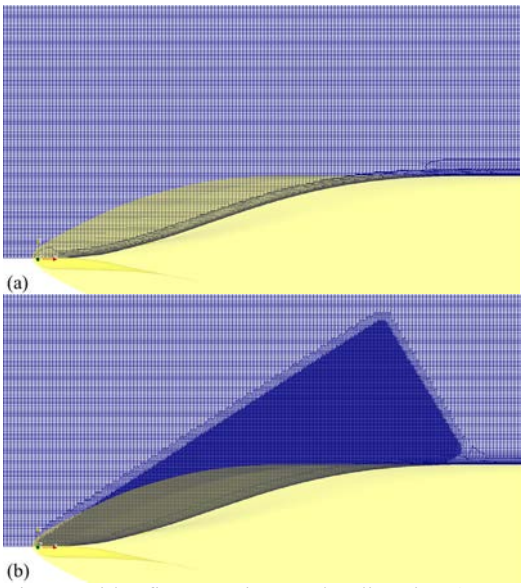


Fig. 6 Grid refinement in x and y direction (a: 16.1million; b: 18.3million)

RESULTS AND ANALYSIS

The computations are carried out on the high-performance computing cluster that consist of 20 cpus per node in Shanghai Jiao Tong University. 40 processors are arranged to calculate the wave breaking cases under different schemes and conditions. It costs approximately 170 hours of clock time to complete the computations.

**Comparison of Resistance and Wave Pattern**

The focus of the present study is on the effects of grid scale on the resolution of bow wave breaking of KCS. The simulation case for Fr=0.35 is under ship speeds of $U = 2.701 m/s$ and the ship model is fixed without the sinkage and trim. The three grid schemes mentioned in
Table 2 are adopted in the simulations. Fig. 7 shows the time history of resistance obtained by the three grid schemes. As we can see, the time history curves of total resistance of KCS at Fr=0.35 are almost the same. The comparison of resistance is presented in Table 3 in which the error is obtained based on the resistance in the 18.3 million grid scheme. The error of resistance among the three grid schemes is within 0.6%. The results show the effect of grid scale on the resistance of KCS at Fr=0.35 is very little at such high computational grids.

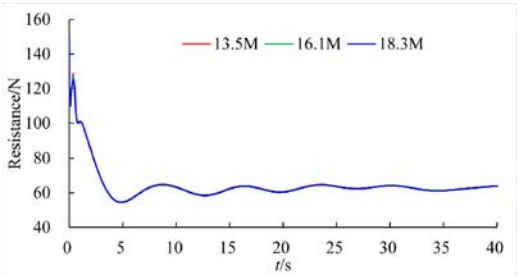


Fig. 7 Time history of resistance

Fig. 8 and Fig. 9 show the wave profiles on the hull surface and wave pattern on the different cuts ($y/L$ = 0.0741, 0.1509, 0.4224). As shown in Fig. 8, the wave profiles on the hull surface obtained by the three schemes are the same basically except for the deviation of the bow wave (about $x/L$=0.25). Fig. 9 presents the local wave patterns of free surface from the near field to the far field in $y$ direction. The wave patterns on these planes are obtained by dividing the wave height by the ship length $L$. At $y/L$=0.0741 and 0.1509, the variation of wave patterns downstream is the same in addition to the deviation near the bow wave. At $y/L$=0.4224, even though there is the slight deviation between the amplitudes of the wave, the wave profiles obtained through the three grid schemes are consistent.

The resistances obtained by the three grid schemes are the same basically. In addition, the wave patterns from near field to far field are also consistent with each other. So, the results show that the three grid schemes adopted in the present work are reliable and robust.

Table 3 Comparison of resistance in different grids

| Grid scheme | Resistance/N | Error |
|---|---|---|
| 13.5Million | 62.785 | 0.524% |
| 16.1Million | 62.592 | 0.215% |
| 18.3Million | 62.458 | - |

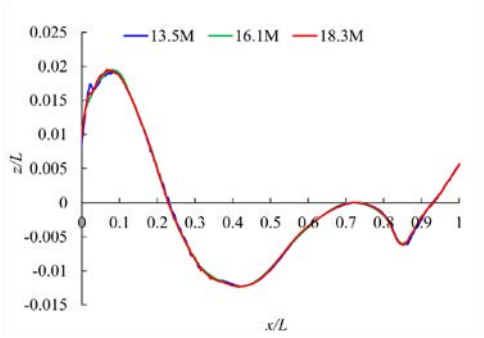

Fig. 8 Wave profiles on hull surface

**Refinement in *z* Direction**

Fig. 10 presents the bow wave patterns by refining the grid in z direction. The top and bottom are the results obtianed by the 13.5million and the 16.1million grids schemes, respectively. As we can see, the refinement in *z* direction is not helpful to capture the breaking of bow wave. Downstream the dotted line, the amplitude at the tail of bow wave via the 13.5 million grids scheme is captured better than that via the 16.1 million grids scheme.

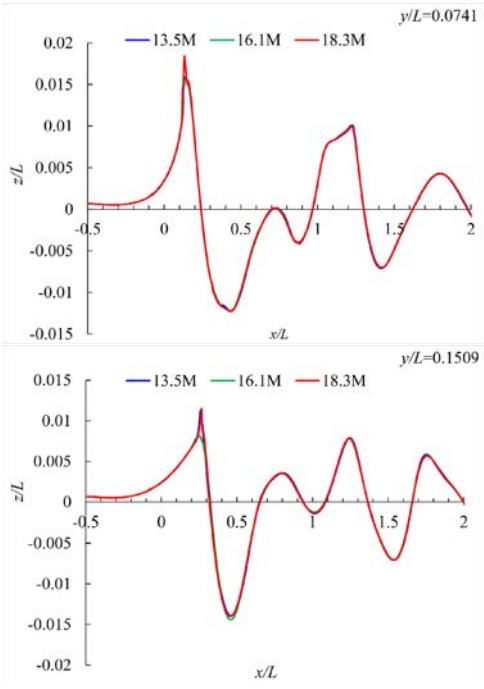


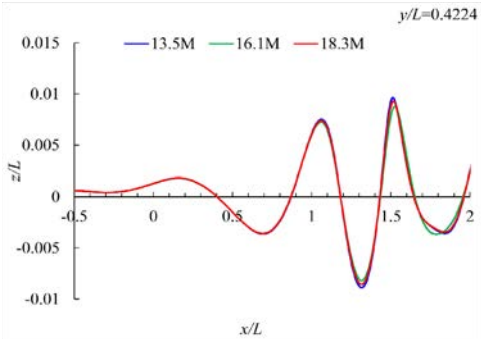

Fig. 9 Comparison of free-surface cuts between different grid schemes.

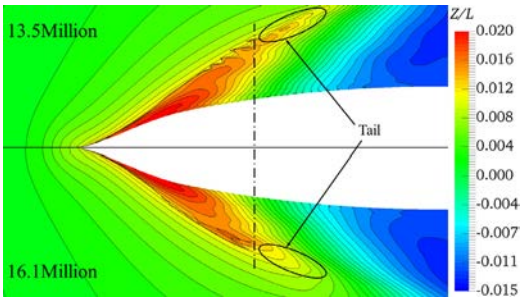

Fig. 10 Comparison of bow wave

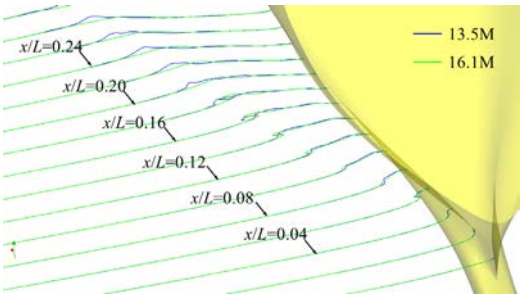

Fig. 11 Wave profiles at different cuts

To explain the evolution of bow wave downstream, the wave profiles in a series of planes are presented in Fig. 11. At the initial position of bow wave, $x/L$=0.04, the wave patterns obtianed by the 13.5 million and 16.1 million grids schemes are approximately the same. The plunger is captured better at $x/L$=0.16 through the refinement in *z* direction while the overturning and the scar of bow wave are not captured. In these two grid schemes, the reconnection of the initial plunger with the free surface is invisible. At the tail of bow wave, $x/L$=0.20 and 0.24, the amplitude of the bow wave obtained by the 13.5 million grids scheme is larger than that obtained by the 16.1 million girds scheme. This result may indicate that the cube grid is better to capture the variation of the ship bow wave.

**Refinement in *x* and *y* Direction**

Fig. 12 presents the bow wave pattern by refining the grid in *x* and *y* direction. The top and bottom are the results obtained by

the 16.1 million and the 18.3 million grids schemes, respectively. The refinement in $x$ and $y$ direction not only makes the breaking of bow wave be captured better but also the scar generated by the overturning of the initial plunger is visible clearly. The result shows the refinement in $x$ and $y$ direction is necessary to simulate the wave breaking of ship at high speed.

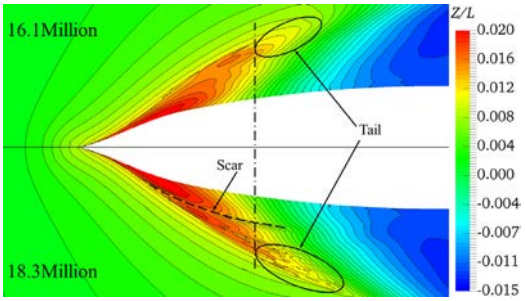

Fig. 12 Comparison of bow wave

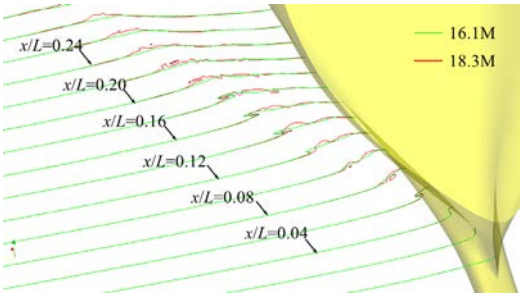

Fig. 13 Wave profiles at different cuts

Fig. 13 shows the evolution of bow wave downstream obtained by refining the grid in $x$ and $y$ direction. These two grid schemes, 16.1million and 18.3million grids schemes, are able to capture the initial plunger that has been formed at $x/L$=0.06. While the reconnection of the initial plunger with the free surface below at $x/L$=0.08 is not captured via the 16.1million grids scheme, the realization is achieved via the 18.3million grids scheme. Even though the plunger is visible clearly at $x/L$=0.12 and 0.16 in these two grid schemes, the evolution of bow wave outboard is not discovered via the 16.1millioin grids scheme. At $x/L$=0.20 and 0.24, the discontinuities and strong non-linear phenomenon of bow wave are appeared in the simulation of 18.3million grids scheme; however, the wave pattern achieved by the 16.1million grids scheme is linear.

**Preliminary Analysis of Bow Wave**

In this section, the preliminary analysis of bow wave obtained by the 18.3 million grids scheme is conducted. The layouts of bow wave in a series of planes are presented in Fig. 14. The scar generated by the overturning of the initial plunger is visible at $x/L$=0.08 and is gradually fuzzy downstream, as shown by the dashed line. The plunger presented by the dotted line is the second plunger that is generated when the scar develops outboard. But the second plunger is not fully developed.

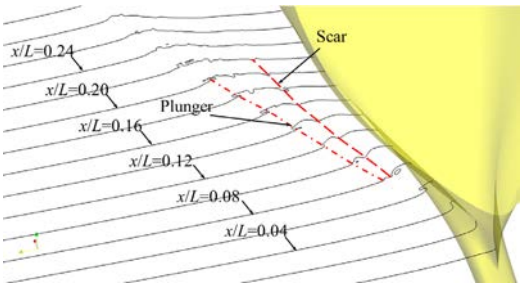

Fig. 14 Evolution of bow wave

Fig. 15 presents the axial vorticity at $x/L$=0.065, 0.085 and 0.145, respectively. As shown in Fig. 15(a), the Pt.A represents the initial plunger that is generated due to the interaction between gravity and inertial forces. The reconnection between the initial plunger and the free surface below (represented by Pt.B) will happen along with the development of initial plunger outboard. In the high curvature region of the overturning wave, the negative axial vorticity (labeled as vortex V1) is generated in the process that the initial plunger is falling. When the tip of initial plunger reconnects with the free surface below, air will be entrained, as shown in Fig. 15(b), resulting in more complex phenomena.

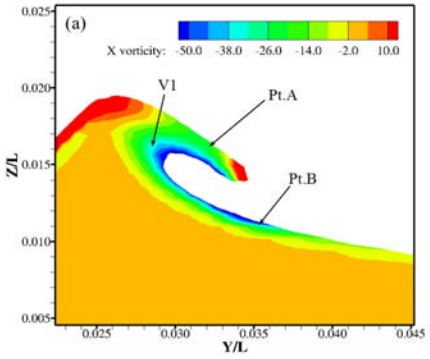


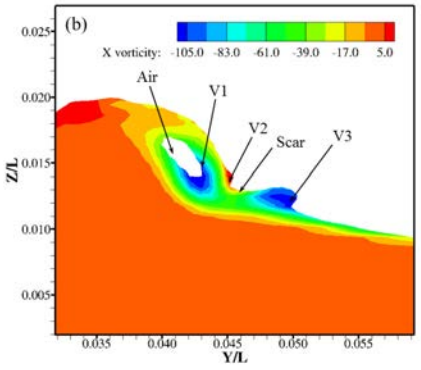

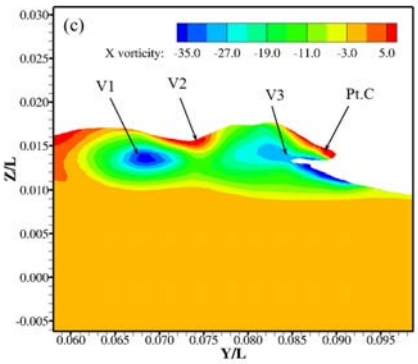


Fig. 15 Axial vorticity distribution, (a): $x/L$=0.065; (b): $x/L$=0.085; (c): $x/L$=0.145.

The generation of the counter-rotating vortex pair (V2 and V3) at $x/L$=0.085 is responsible for the scar where the positive vorticity (V2) is generated and the second plunger visible at $x/L$=0.085, Pt.C in Fig. 15(c). When the tip of the initial plunger reconnects with the free surface below, the interaction between the two parts causes the upward motion of fluid resulting in the positive vorticity and scar and the negative vorticity (V3) is generated at the toe. The vortex pair that has a rotating orientation pumps fluid outboard resulting in the second plunger. The air entrainment is observed at $x/L$=0.085 in the process of the overturning of the initial plunger. At $x/L$=0.145, the air entrainment is not visible while the second plunger (Pt. C) is observed clearly.

## CONCLUSION

In the present work, an exploratory study of grid scale on the wave breaking of KCS under high speed is performed. The refinement in different directions is conducted to study the effect on the bow wave breaking. When the ratio of the grid scale to $L_{pp}$ is about 1.56e-3, the bow wave breaking is captured better. The refinement only in $z$ direction is not able to capture the phenomena of bow wave breaking. While the wave breaking of bow wave of KCS is visible clearly through the refinement in $x$ and $y$ direction. The overturning and breaking of bow wave is observed clearly and also the air entrainment and scar are noticeable. In the process of the overturning of bow wave, the variation of vorticity is concentrated near the free surface. The counter-rotating vortex generated by the reconnection of the initial plunger with the free surface below is responsible for the second plunger and scar. In the present study, the reference of grid scale to simulate the wave breaking is provided. But the use of the present scheme does not allow for a very elaborate simulation of bow wave breaking. So, in the future work, smaller grid size may be adopted. In addition, the phenomenon of air entrainment that is captured roughly in the present study should be paid more attention, such as, the evolution downstream and outboard.

## ACKNOWLEDGMENTS

This work is supported by the National Natural Science Foundation of China (51490675, 11432009, 51579145), Chang Jiang Scholars Program (T2014099), Shanghai Excellent Academic Leaders Program (17XD1402300), Program for Professor of Special Appointment (Eastern Scholar) at Shanghai Institutions of Higher Learning (2013022), Innovative Special Project of Numerical Tank of Ministry of Industry and Information Technology of China (2016-23/09) and Lloyd's Register Foundation for doctoral student, to which the authors are most grateful.

## REFERENCES

Berberović, E, van Hinsberg, NP, Jakirlić, S, Roisman, IV, and Tropea, C (2009). "Drop impact onto a liquid layer of finite thickness: dynamics of the cavity evolution," *Phys Rev E*, 79(3), 36306.

Dong, R, Katz, J, and Huang, T (1997). "On the structure of bow waves on a ship model," *J Fluid Mech*, 346, 77-115.

Duncan, HJ (1983). "The breaking and non-breaking resistance of a two-dimensional hydrofoil," *J Fluid Mech*, 126, 507-520.

Liu, C, Wang, J, Wan, D, and Yu, X (2017a). "Computation of Wave Drift Forces and Motions for DTC Ship in Oblique Waves," *Proc 27th Int Ocean Polar Eng Conf*, San Francisco, USA, 144-152.

Liu, C, Wang, J, and Wan, D (2017b). "The Numerical Investigation on Hydrodynamic Performance of Twisted Rudder during Selfpropulsion," *Proc 8th Int Conf Comput Methods*, Guilin, China, 934-943.

Marrone, S, Colagrossi, A, Antuono, M, Lugni, C, and Tulin, M (2011). "A 2D+t SPH model to study the breaking wave pattern generated by fast ships," *J Fluids Structures*, 27, 1199-1215.

Marrone, S, Bouscasse, B, Colagrossi, A, and Antuono, M (2012). "Study of ship wave breaking patterns using 3D parallel SPH simulations," *Comput Fluids*, 69, 54-66.

Menter, FR, Kuntz, M, Langtry, R (2003). "Ten years of industrial experience with the SST turbulence model, Turbulence," *Turbul Heat Mass Transf*, 4(1), 625-632.

Noblesse, F, Delhommeau, G, Liu, H, Wan, DC, and Yang, C (2013). "Ship bow waves," *J Hydrodyn Ser B*, 25(4), 491-501.

Ogilvie, F (1972). "The wave generated by a fine ship bow," *9th Symp Nav Hydrodyn*, Paris, France, 1483–1524.

Olivieri, A, Pistani, F, Wilson, R, Campana, EF, and Stern, F (2007). "Scars and Vortices Induced by Ship Bow and Shoulder Wave Breaking," *J Fluids Eng*, 129, 1445-1459.

Roth, GI, Mascenik, DT, and Katz, J (1999). "Measurements of the flow structure and turbulence within a ship bow wave," *Phys Fluids*, 11, 3512-3523.

Rusche, H (2003). "Computational fluid dynamics of dispersed two-phase flows at high phase fractions," Ph.D. Thesis, Imperial College, London, UK.

Wang, J, and Wan, D (2017). "Breaking Wave Simulations of High-speed Surface Combatant using OpenFOAM," *Proc 8th Int Conf Comput Methods*, Guilin, China, 841-852.

Waniewski, TA, Brennen, CE, and Raichlen, F (2002). "Bow wave dynamics," *J Ship Res*, 46, 1-15.

Weller, H and Weller, H (2008). "A high-order arbitrarily unstructured finite-volume model of the global atmosphere: Tests solving the shallow-water equations," *Int J Numer Methods Fluids*, 56(8), 1589-1596.

Wilson, RV, Carrica, PM, and Stern, F (2006). "URANS simulations for a high-speed transom stern ship with breaking waves," *Int J Comput Fluid Dyn*, 20(2), 105-125.

Xia, K, and Wan, D (2017a). "Effects of wave steepness on wave breaking properties over submerged reef," *Proc 8th Int Conf Comput Methods*, Guilin, China, 952-961.

Xia, K, Ai, Y, and Wan, D (2017b). "Hydrodynamic Study of Wave Evolution Characteristics around Semi-submersible Platform in Shallow Water with Submerged Terrain near Island," *Proc 27th Int Ocean Polar Eng Conf*, San Francisco, USA, 161-169.